Eur. Phys. J. D **17**, 307–318 (2001)

THE EUROPEAN PHYSICAL JOURNAL D

EDP Sciences

Kinematically complete final state investigations of molecular photodissociation: two- and three-body decay of laser-prepared H_3 3s $^2A_1'$

U. Galster, P. Kaminski, M. Beckert, H. Helm, and U. Müller[a]

Fakultät für Physik, Albert-Ludwigs-Universität Freiburg, Hermann-Herder-Strasse 3, 79104 Freiburg, Germany

Received 29 March 2001

Abstract. We have performed kinematically complete investigations of molecular photodissociation of triatomic hydrogen in a fast beam translational spectrometer recently built in Freiburg. The apparatus allows us to investigate laser-induced dissociation of neutral molecules into two, three, or more neutral products. The fragments are detected in coincidence and their vectorial momenta in the center-of-mass frame are determined. We demonstrate the potential of the method at the fragmentation of the $3s\ ^2A_1'(N=1,K=0)$ state of triatomic hydrogen. In this state, three-body decay into ground state hydrogen atoms H+H+H, two-body predissociation into $H+H_2(v,J)$, and photoemission to the H_3 ground state surface with subsequent two-body decay are competing channels. In the case of two-body predissociation, we determine the rovibrational population in the $H_2(v,J)$ fragment. The vibrational distribution of H_2 is compared with approximate theoretical predictions. For three-body decay, we measure the six-fold differential photodissociation cross-section. To determine accurate final state distributions, the geometric collection efficiency of the apparatus is calculated by a Monte Carlo simulation, and the raw data are corrected for apparatus efficiency. The final state momentum distribution shows pronounced correlation patterns which are characteristic for the dissociation mechanism. For a three-body decay process with a discrete kinetic energy release we have developed a novel data reduction procedure based on the detection of two fragments. The final state distribution determined by this independent method agrees extremely well with that observed in the triple-coincidence data. In addition, this method allows us to fully explore the phase space of the final state and to determine the branching ratios between the two- and three-body decay processes.

PACS. 33.80.Gj Diffuse spectra; predissociation, photodissociation – 33.80.Rv Multiphoton ionization and excitation to highly excited states (e.g., Rydberg states) – 34.80.Ht Dissociation and dissociative attachment by electron impact

1 Introduction

Neutral triatomic hydrogen plays the role of a prototype to study molecular fragmentation dynamics. Rydberg states of H_3 exist [1–6]. Their bound potential energy surfaces are embedded in the continuum of the repulsive ground state surface. They can undergo radiative as well as predissociative decay: two-body predissociation into $H(1s)+H_2(v,J)$ fragment pairs, three-body breakup into three neutral hydrogen atoms $H(1s)+H(1s)+H(1s)$, and radiative decay with subsequent two- and three-body dissociation [7–13]. Metastable H_3 molecules prepared in a fast beam by charge transfer neutralization of H_3^+ serve as a platform for laser-excitation processes. Rydberg states well-characterized in all quantum numbers can be populated, and their decay into neutral products can be studied using time and position-sensitive detectors.

The predissociation of laser-prepared H_3 into $H+H_2(v,J)$ fragment pairs has been investigated by translational spectroscopy [7,9]. In these double-coincidence experiments, evidence for three-body decay was found [10]. Extensive modelling was required to gain insight into the final state distributions. Triple coincidence studies of the fragmentation of H_3 into neutral hydrogen atoms $H(1s)+H(1s)+H(1s)$ were first performed in Freiburg [11]. A novel photofragment spectrometer [12] was developed which allows us to measure the positions and arrival time differences of all fragments using multi-hit time- and position-sensitive detectors [14,15]. New data reduction algorithms [13] were developed to determine the momentum vectors of the fragments in the center-of-mass frame from the measured quantities.

The objective of this paper is to determine the branching between the two- and three-body decay mechanisms of H_3, and to measure kinematically complete final state distributions. We report a detailed analysis of the

[a] e-mail: Ulrich.Mueller@uni-freiburg.de

$3s\ ^2\mathrm{A}_1'(N=1,K=0)$ state. The method, however, can be applied to systematically investigate all laser-excited bound states of H_3. The geometric collection efficiency of the apparatus for the different processes is calculated by a Monte Carlo simulation, and corrections are applied to the measured distributions. We have developed a novel algorithm to evaluate three-body events from double-hits. This allows us to explore the complete phase space accessible in the final state distribution and to determine the branching between two- and three-body decay without knowing the absolute electronic detector efficiency.

A comparison of the initial- and final-state resolved experimental data with the results of two-dimensional wavepacket calculations [16,17] gives insight into the coupling mechanisms between the excited and ground state surfaces in the regime of the breakdown of the Born-Oppenheimer approximation. These mechanisms play an important role in the dissociative recombination of H_3^+ with electrons where two-body as well as three-body product states have been detected experimentally [18].

2 Experimental

In the Freiburg photofragment spectrometer [11,12], a fast beam (3 to 6 keV) of mass selected H_3^+ ions is neutralized by charge transfer in cesium. The remaining ions are removed from the neutral beam by an electric field. Products of dissociative charge transfer are stopped in a distance of about 30 cm from the charge transfer cell, where a well-collimated beam of metastable H_3 $2p\ ^2\mathrm{A}_2''(N=K=0)$ molecules is skimmed by an aperture of 300 μm diameter. The metastable beam is excited in the cavity of a standing wave dye laser. The photofagments which separate from each other due to their kinetic energy in the center-of-mass frame are detected in coincidence by a time- and position-sensitive multi-hit-detector after a free-flight of about 150 cm. The undissociated part of the neutral beam is intercepted by a tiny beam flag in a distance of about 10 cm from the laser interaction region.

The detector for fast neutral fragments consists of two Z-stacks of multichannel plates (MCP) with an active area of 40 mm diameter and position sensitive delay line anodes [14,15]. Electromagnetic pulses are induced on a system of waveguides by the electron charge clouds from the MCP's. The hit coordinates are determined by measuring the arrival time differences of the pulses at the waveguide terminals using time-to-digital (TDC) converters. Pulses derived from the voltage drop at the MCP's are used to determine the arrival time differences of the fragments. Pulse routers to distribute the pulses of consecutive events to different TDC input channels are provided for all position- and timing signals. An *in situ* calibration of the position measurement is performed using a stainless steel mask with a pattern of circular holes which is placed in front of the detector and "illuminated" by fast fragments. As shown in Figure 1a, we have the choice between two detector orientations in the laboratory frame:

(A) with the sensitive detector regions (MCP's) centered on the z-axis of the laboratory frame,

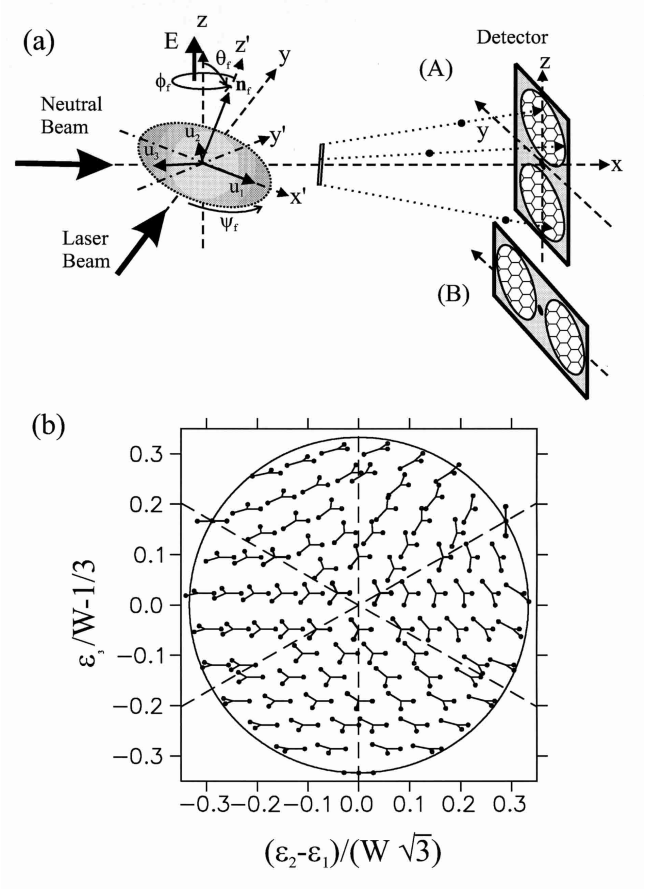

Fig. 1. Projection of the six-fold differential cross-section for three-body decay. (a) Orientation of the plane containing the c.m. fragment momenta. (A) and (B) show the two detector geometries relative to the neutral molecular and laser beam. (b) Dalitz plot. The symbols show the correspondence between the configuration of the fragment momenta in the plane with respect to each other and the location in the plot.

(B) and with the detector rotated by 90° about the x-axis (fast beam axis) such that the MCP's are centered on the y-axis.

3 Excitation

The anisotropy in the distribution of the photofragments may be strongly correlated with the alignment of the nuclear frame of H_3 induced by the laser excitation. In the following, we analyze the angular distribution of the molecular top axis in the laser-excited $3s\ ^2\mathrm{A}_1'(N=1,K=0)$ state of H_3. We follow reference [19] and expand the angular part of the Hund's case b wave function Ψ (disregarding the vibrational and spin wavefunctions) in terms of Hund's case d wave functions γ:

$$\Psi_{\lambda KM}^{LN} = \sum_{N^+} \gamma_{NM}^{LN^+K^+} (-1)^{L-\lambda} \langle L\lambda, N-K | LNN^+ - K^+ \rangle \times \left[(1+\delta_{K^+0})/(1+\delta_{\lambda 0}\delta_{K^+0})\right]^{1/2} \quad (3.1)$$

$$K = \lambda + K^+. \quad (3.2)$$

The expressions in brackets $\langle|\rangle$ are Clebsch Gordan coefficients. In Hund's case b, good quantum numbers are the total angular momentum N (disregarding electron spin), the electronic angular momentum L, their projections K and λ on the body-fixed axis, and the projection M of the total angular momentum on the space-fixed axis. Hunds case d wave functions are constructed by attaching an electron wave function $Y_{Lm}(\Omega_e)$ with angular momentum L and projection m on the space-fixed quantization axis to the wave function of the H_3^+ ion core

$$\gamma_{NM}^{LN^+K^+} = \sum_m Y_{Lm}(\Omega_e) D^{N^+}_{K^+M^+} \times \langle Lm, N^+M^+ | LN^+NM\rangle \quad (3.3)$$

$$M = m + M^+. \quad (3.4)$$

To describe the ionic nuclear frame, we use symmetric top wave functions $D^{N^+}_{K^+M^+}$ with total angular momentum N^+ and projections K^+ and M^+ on the body- and space-fixed axes, respectively (Eq. (4.1.12) in Ref. [25]). They depend on the Euler angles (ϕ, θ, χ):

$$D^{N^+}_{K^+M^+}(\phi,\theta,\chi) = \mathrm{e}^{\mathrm{i}K^+\chi}\; d^{N^+}_{K^+M^+}(\theta)\; \mathrm{e}^{\mathrm{i}M^+\phi}. \quad (3.5)$$

The functions $d^{N^+}_{K^+M^+}(\theta)$ can be expressed by the Jakobi polynomials $P(\cos\theta)$ (Eq. (4.1.23) in Ref. [25])

$$d^{N^+}_{K^+M^+}(\theta) = \left[\frac{(N^+ + K^+)!(N^+ - K^+)!}{(N^+ + M^+)!(N^+ - M^+)!}\right] \times \cos(\theta/2)^{K^+ + M^+} \sin(\theta/2)^{K^+ - M^+} \times P^{(K^+-M^+, K^+ + M^+)}_{N^+ - K^+}(\cos\theta) \quad (3.6)$$

The selection rules for excitation of vibrationless H_3 $2p\ ^2A_2''$ ($N''=0, K''=0$) molecules into the $3s\ ^2A_1'$ state (parallel transition) by linearly polarized laser light are [1]

$$\begin{aligned} \Delta N &\equiv N' - N'' = 1, \\ \Delta K &\equiv K' - K'' = 0, \\ \Delta M &\equiv M' - M'' = 0. \end{aligned} \quad (3.7)$$

The quantum numbers of the excited state are $N' = 1$, $K' = 0$, $M' = 0$. Because the electronic angular momentum L and the projections (λ, m) vanish in the $3s\ ^2A_1'$ state, Hund's cases b and d wave functions are identical, and the final state wave function is

$$\Psi^{01}_{000}(3s) = Y_{00}(\Omega_e) D^1_{00}(\phi,\theta,\chi). \quad (3.8)$$

The probability distribution of finding the molecular top axis pointing into the solid angle element $\mathrm{d}\Omega = \mathrm{d}\phi\,\sin\theta \mathrm{d}\theta\,\mathrm{d}\chi$ is given by the absolute square of the wave function integrated over the electronic coordinates Ω_e:

$$P_{3s}(\theta)\mathrm{d}\Omega = \mathrm{d}\Omega \int \mathrm{d}\Omega_e \left|\Psi^{01}_{000}\right|^2 \quad (3.9)$$

$$= \left|d^1_{00}(\theta)\right|^2 \mathrm{d}\Omega \int \left|Y_{00}(\Omega_e)\right|^2 \mathrm{d}\Omega_e = \cos^2\theta \mathrm{d}\Omega. \quad (3.10)$$

Consequently, the molecular top axis is aligned with a $\cos^2\theta$ distribution with respect to the laser polarization.

It is instructive to analyze the angular distribution of the molecular top axis in the H_3 $2p\ ^2A_2''$ ($N = K = M = 0$) metastable state. The electronic angular momentum is $L = 1$. In the Hund's case b basis, the projection of L on the body-fixed axis is $\lambda = 0$. According to the selection rule (Eq. (3.2)), the projection of the core angular momentum on the body-fixed axis vanishes ($K^+ = 0$). The only non-vanishing Clebsch-Gordan coefficient in equation (3.1) is that with $N^+ = 1, K^+ = 0$. In the $2p\ ^2A_2''$ metastable state, Hund's cases b and d wave functions are identical and can be expressed by

$$\Psi^{10}_{000}(2p) = \frac{1}{\sqrt{3}}\left(Y_{1-1}(\Omega_e)D^1_{01} - Y_{10}(\Omega_e)D^1_{00} + Y_{11}(\Omega_e)D^1_{0-1}\right). \quad (3.11)$$

The three magnetic sublevels of the rotor are fully entangled with those of the electronic wave function. By integrating the absolute square of the wave function $\Psi^{10}_{000}(2p)$ over the unobserved electron coordinate making use of the ortho-normality of the spherical harmonics

$$\begin{aligned} P_{2p}(\theta)\mathrm{d}\Omega &= \mathrm{d}\Omega \int \mathrm{d}\Omega_e \left|\Psi^{10}_{000}(2p)\right|^2 \quad (3.12)\\ &= \left(\left|d^1_{01}(\theta)\right|^2 + \left|d^1_{00}(\theta)\right|^2 + \left|d^1_{0-1}(\theta)\right|^2\right)\mathrm{d}\Omega \\ &= \left(\left|-\sin(\theta)/\sqrt{2}\right|^2 + \left|\cos(\theta)\right|^2 + \left|\sin(\theta)/\sqrt{2}\right|^2\right)\mathrm{d}\Omega \\ &= 1\ \mathrm{d}\Omega \end{aligned}$$

we find an isotropic angular distribution $P_{2p}(\theta)$ of the molecular top axis in the metastable state of H_3. Note that the $2p\ ^2A_2''$ ($N = K = 0$) state is a pure quantum state. The angular distribution in the metastable beam remains isotropic although the population is reduced in the laser-excitation.

4 Results

4.1 Triple coincidences following photodissociation of H_3 $3s\ ^2A_1'$

4.1.1 Data projection and Monte Carlo simulation

For each triple coincidence produced by three-body decay of H_3, we determine the c.m. fragment velocity vectors $\mathbf{u}_i$ (see Refs. [11–13]). To gain insight into the fragmentation dynamics, the six-fold differential cross-section is projected as shown in Figure 1. In the c.m. frame, the vectors $\mathbf{u}_i$ are contained in a plane. For each event, we define a new coordinate system (x', y', z') by the normal vector $\mathbf{n}_\mathrm{f} = (\mathbf{u}_1 \times \mathbf{u}_2)/(u_1 u_2)$ on this plane (z'-axis) and by the direction of the largest momentum vector observed (x'-axis).

As shown in Figure 1a, three Euler angles $(\psi_f, \theta_f, \phi_f)$ describe the orientation of the (x', y', z')-coordinate system within the laboratory reference frame (x, y, z), defined by the electric vector of the laser beam (z-axis) and the direction of the neutral beam (x-axis). For the remaining three parameters, we define the fragment energies in the c.m. frame by $\epsilon_i = m\mathbf{u}_i^2/2$ and use the total kinetic energy $W = \epsilon_1 + \epsilon_2 + \epsilon_3$. To visualize the correlation among the fragment momenta in the (x', y') plane, we use a Dalitz plot [23] which conserves the phase space density. We plot for each event $(\epsilon_3/W - 1/3)$ *vs.* $((\epsilon_2 - \epsilon_1)/(W\sqrt{3}))$. Energy and momentum conservation require that the data points lie inside a circle with radius 1/3, centered at the origin. The correspondence between the configuration of the fragment momenta and the location in the plot is shown in Figure 1b. The threefold rotation symmetry around the origin and the mirror symmetry with respect to the dashed lines in Figure 1b result from the equal masses of the fragments.

To determine the geometric collection efficiency of the apparatus, we have performed Monte Carlo simulations. We calculate random fragment velocity vectors $\mathbf{u}_i$ corresponding to the three-body kinetic energy release of the H_3 $3s$ $^2A_1'(N = 1, K = 0)$ state with a homogeneous density in the kinematically accessible space of the (x', y') plane. The angles ϕ_f and ψ_f have uniform distributions within $[0, 2\pi]$. The probability distribution of the angle θ_f is parameterized by

$$P(\cos\theta_f) = [1 + \beta_f(3\cos^2\theta_f - 1)/2]/(4\pi) \qquad (4.1)$$

with the alignment parameter β_f [24]. The special values $\beta_f = 2$, 0, and -1 correspond to $\cos^2\theta_f$, isotropic, and $\sin^2\theta_f$ distributions, respectively. From the c.m. fragment velocities and the known primary beam energy and divergence, we calculate the trajectories of the fragments. Acceptance of an event as a triple hit is modeled depending on the position and size of the beam flag, the detector geometry, and the finite pulse pair resolution. The positions and arrival time differences of the fragments at the detector are determined taking into account the uncertainties in the time- and position-measurements. The further processing of the simulated data is identical to that in the measurements.

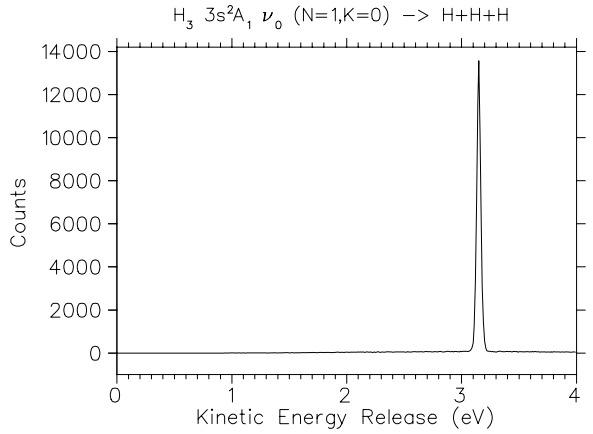

Fig. 2. Measured kinetic energy release in three-body decay of the H_3 $3s$ $^2A_1'$ state into ground state atoms.

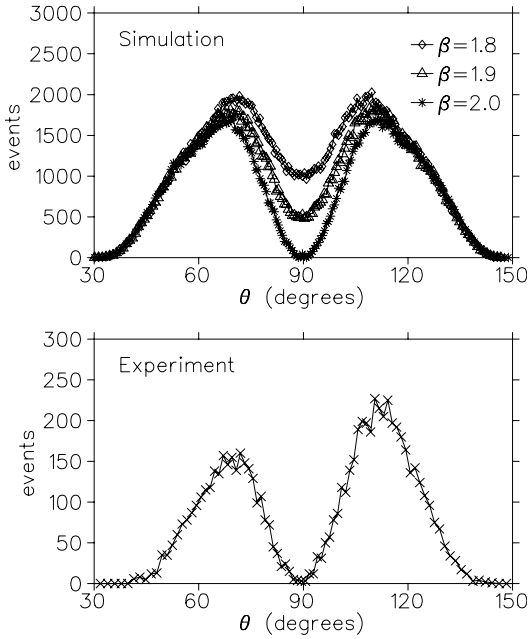

Fig. 3. Alignment of the normal vector $\mathbf{n}_f$ in three-body decay of vibrationless H_3 $3s$ $^2A_1'(N = 1, K = 0)$. Lower panel: experimental data. The detector was oriented in position (A). Upper panel: results of a Monte Carlo simulation for randomly distributed fragmentation configurations and for alignment parameters of $\beta = 1.8$, 1.9, and 2.0.

4.1.2 Kinetic energy release and angular distribution

The spectrum of the total c.m. kinetic energy release W poses a stringent test on the quality and precision of our data-acquisition and -reduction procedure. Since the energy of the laser-excited initial state above the three-body limit is laser-selected, W has to appear as a discrete observable. Figure 2 shows the kinetic energy release spectrum from triple coincidence data of the vibrationless H_3 $3s$ $^2A_1'(N = 1, K = 0)$ initial state binned at 10 meV resolution. A narrow peak appears at 3.17 eV which is very close to the known energy of the initial state [7] above the three-body limit, 3.155 eV. Radiative processes to the lower states (*e.g.* $3p$ E′, $2p$ A_2'' or the $2p$ E′ ground state surface) with subsequent three-body decay play a minor role in the case of H_3 $3s$ $^2A_1'(N = 1, K = 0)$ as evidenced by the absence of background to the distribution in Figure 2.

The alignment of the molecular top axis of H_3 with $P(\theta)\mathrm{d}\Omega = \cos^2\theta\mathrm{d}\Omega$ with respect to the laser polarization (see Sect. 3) produces a non-isotropic distribution in the final state. For a set of triple coincidences, we have determined the angle θ_f between the normal vector $\mathbf{n}_f$ on the plane containing the c.m. fragment velocity vectors $(\mathbf{u}_1, \mathbf{u}_2, \mathbf{u}_3)$ and the laser polarization (z-axis). The measured distribution of θ_f is shown in the lower panel of Figure 3. In this measurement, the detector was in position (A) with the sensitive regions centered on the z-axis

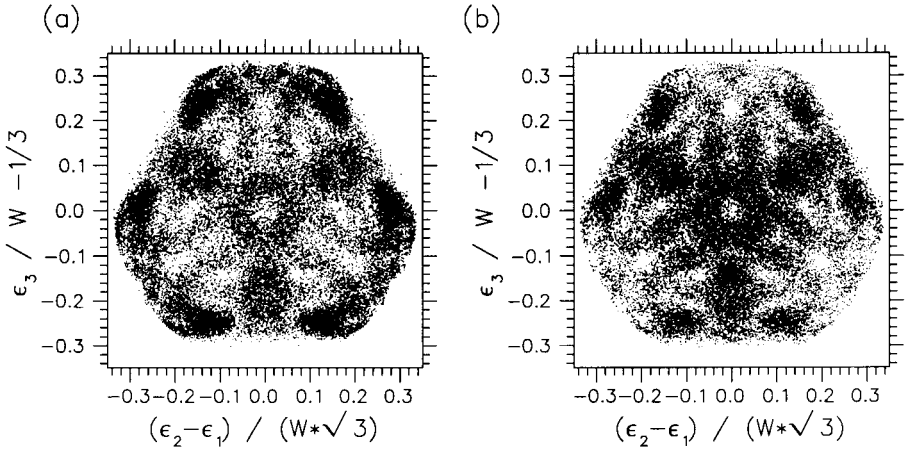

Fig. 4. Triple coincidences from three-body decay of vibrationless H_3 $3s\ ^2A_1'(N=1,K=0)$. The experimental data are shown in a Dalitz plot. In (a) and (b), the detector was oriented in positions (A) and (B), respectively (see Fig. 1).

(see Fig. 1). The calculated distributions of the angle θ_f for initial values β_f =1.8, 1.9, and 2.0 of the alignment parameter [*cf.* Eq. (4.1)] are shown in the upper panel of Figure 3. Between $\theta_f = 0°$ and $\theta_f = 30°$ and between $\theta_f = 150°$ and $\theta_f = 180°$, the distributions vanish due to the finite geometric collection efficiency of the detector. Our simulations show that the signal at $\theta_f = 90°$ depends most sensitively on the specific value of the alignment parameter. The clear minimum in the experiment at $\theta_f = 90°$ is reproduced by the value $\beta_f = 2^{+0}_{-0.1}$ which corresponds to a $\cos^2\theta_f$ distribution. The alignment of $\mathbf{n}_f$ in the final state is identical to that of the molecular top axis in the laser-prepared initial state (*cf.* Sect. 3). Although a significant amount of angular momentum is transferred from the electrons to the nuclear frame in the radiationless transition from the $3s\ ^2A_1'$ $(L=0)$ to the repulsive $2p\ ^2E'$ $(L=1)$ state, the plane of the fragment momenta is identical to the molecular plane. This shows that the dissociation dynamics on the repulsive surface occurs very fast compared to the rotational period.

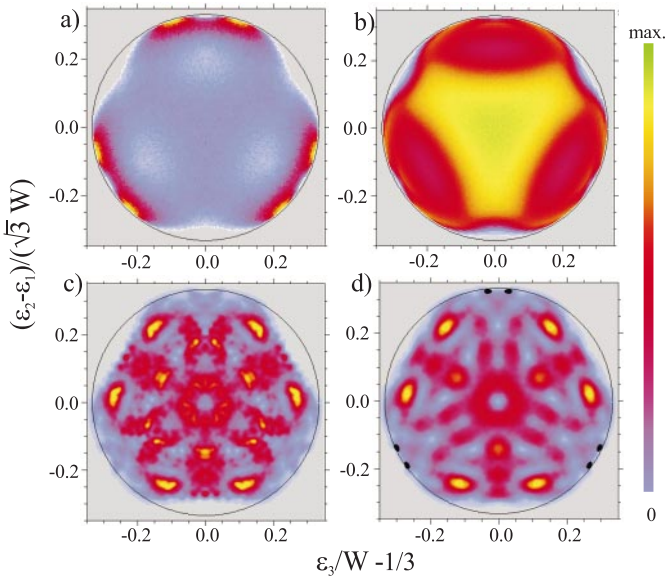

Fig. 5. Final state correlations in the three-body decay of H_3 $3s\ ^2A_1'(N=1,K=0)$. In (a) and (b), triple-hit collection efficiencies are shown for detector orientation in positions (A) and (B), respectively. In (c) and (d), we show the final state distributions of Figures 4a and 4b corrected for the collection efficiencies.

4.1.3 Fragment correlations

To study the correlations among the fragment momenta, the experimental data are shown in a Dalitz plot in Figure 4. The data points for orientations (A) and (B) of the detector in the laboratory frame (*cf.* Fig. 1) are shown in Figures 4a and 4b, respectively. In both figures, regions with high and low point densities are observed. The differences in the intensities of these features result from the geometric collection efficiency of the detector due to the strong alignment in the angular distribution of the $3s\ ^2A_1'(N=1,K=0)$ initial state. The, detection of fragment triples where one of the momenta is close to zero (linear configuration) and therefore hits the space between the two detectors is excluded by our detector geometry. Also, fragment hits which are close in time as well as in space ($H+H_2$ configuration) are suppressed due to the finite pulse pair resolution of the detector. For both detector orientations, we have calculated the collection efficiency as a function of the fragmentation configuration by a Monte Carlo simulation. We find that in orientation (B) the overall detection efficiency is higher than in (A). On the other hand, orientation (A) is very sensitive on the value of the alignment parameter β_f and, therefore, is preferred to determine experimental angular distributions. The collection efficiencies as a function of the fragmentation configuration are shown in Figures 5a and 5b in false color images. These results are used to weight the experimental data points in Figures 4a and 4b. The correct final state distributions are shown as false color images in Figures 5c

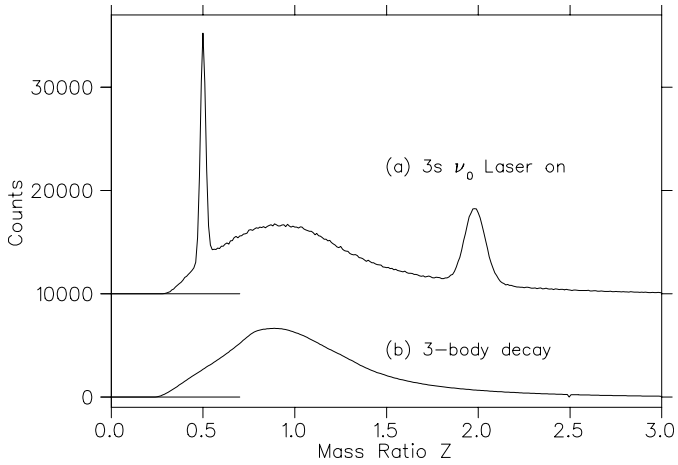

Fig. 6. Double coincidences following fragmentation of H_3 $3s\ ^2A_1'(N=1,K=0)$. (a) Measured spectrum of the mass ratio Z, (b) simulated spectrum of Z resulting from three-body decay.

and 5d. A boxcar smoothing over 7 neighboring pixels was applied to the images. The effect of the smoothing can be judged from the intensity outside the kinematically allowed region (black circle in Figs. 5c and 5d). All islands of low and high point density which have been visible in the raw data in Figure 4 also appear in the corrected distributions. After correction, we find that the intensities of these features are in remarkably good agreement for both detector orientations.

4.2 Double coincidences following photodissociation of H_3 3s $^2A_1'$

Coincident events with one fragment on each sensitive region of the detector can be produced either by two-body decay into H + H_2 or by three-body decay into H(1s)+H(1s)+H(1s) with one fragment missing the detector. In the following, we evaluate two- as well as three-body events contained in a set of double-hit coincidence data. This allows us to determine the branching between both processes, without knowing the absolute electronic detector efficiency. For each event, the hit coordinates $(y_1,z_1),(y_2,z_2)$ and the arrival time difference $\Delta T = t_2 - t_1$ are measured. To distinguish between two- and three-body decay, we determine the quantity Z

$$Z = |(R_1/R_2)\,(1-(v_{0x}\Delta T)/L)| \qquad (4.2)$$

from the velocity v_{0x} of the parent beam, the flight length L, and the distances from the detector center $R_i = \sqrt{y_i^2+z_i^2}$. In the case of two-body decay, Z corresponds to a good approximation to the mass ratio $Z \approx m_2/m_1$. The spectrum of Z is shown in Figure 6a. The events produced by two-body breakup fall into the pronounced peaks at $Z = 1/2$ and $Z = 2$. Because of the momentum carried by the unobserved third hydrogen atom, three-body decay appears in this distribution as a continuous broad feature with a maximum close to $Z = 1$. From the spectrum of the time difference ΔT, we find that the amount of false coincidences is almost negligible. The events fulfilling the condition

$$Z \in [0.45, 0.55] \quad \text{or} \quad Z \in [1.82, 2.22] \qquad (4.3)$$

are accepted as two-body decay. The significance of the trace labelled (b) in Figure 6 will be discussed at the end of Section 4.2.1.

4.2.1 Three-body decay of H_3 evaluated from double coincidences

Events which fail to fulfill condition equation (4.3) are treated as three-body decay events. In Appendix A, we describe an iterative data reduction algorithm to determine the correlations in the final state from the measured coordinates of the fragment hits and the time difference. To make use of momentum conservation, we neglect the small divergence of the metastable beam measured to be about 0.7 mrad FWHM. We further assume that the kinetic energy release is mono-energetic and that it's value W is determined by the energy gap between the H_3 $3s\ ^2A_1'(N=1,K=0)$ initial state and the three-atom limit [10,11] (no photoemission). We determine the (apparent) fragment velocity vectors $\mathbf{u}_i$ by the algorithm described in Appendix A. This equation system is under-determined, and the sign of the longitudinal velocity component of one of the fragments is chosen arbitrarily to be positive. Still, about half of the events are evaluated correctly. We project the distribution of the apparent fragment velocity vectors as described in Section 4.1.1. The alignment of the angle θ_f is found to be consistent with the observations in Section 4.1.2. For each event, we determine the apparent c-m fragment energies $E_i = m\mathbf{u}_i^2/2; i = 1\ldots3$. To avoid saturation of the image, only the first 60.000 of the available 850.000 data points are shown in a Dalitz plot in Figure 7a. The observed distribution is a convolution of the photofragmentation cross-section with the experimental uncertainties induced by the finite size of the interaction region, the primary beam divergence, and the unknown sign in the data reduction procedure. Nevertheless, we observe islands of high and low point densities which correspond closely to those observed in the direct triple-hit experiment in Figure 4. The events evaluated with the incorrect sign produce an almost homogeneous background in Figure 7a.

For practical reasons, we re-number the fragments of each event such that $E_1 \le E_2 \le E_3$ and accumulate them in a two-dimensional distribution of the energy ratios $A = E_1/W$ and $B = E_2/W$. Figure 7b shows the histogram of the measured data $X_m(A,B)$ in a plot of B *vs.* A. The kinematically accessible region in this plot is marked by dashed lines. To determine the correct final state distribution of the photofragmentation, we fit the measured distribution $X_m(A,B)$ with a set of basis functions $X_b(A,B;\epsilon_1,\epsilon_2)$

$$X_m(A,B) = \sum_{\epsilon_1,\epsilon_2} a(\epsilon_1,\epsilon_2) X_b(A,B;\epsilon_1,\epsilon_2). \qquad (4.4)$$

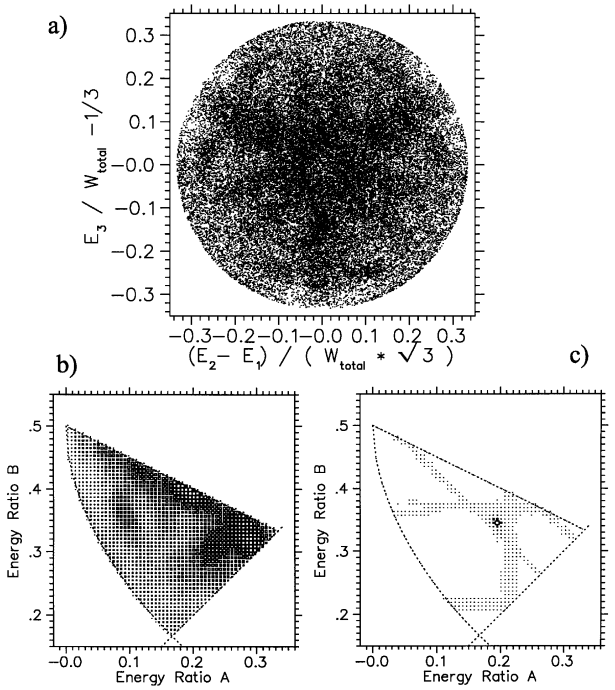

Fig. 7. Three-body decay of H_3 $3s\ ^2A_1'(N = 1, K = 0)$ evaluated from double-coincidences. The Dalitz plot (a) shows the first 60.000 events of the measured data set. The data reduction is described in Appendix A. In (b), all events are accumulated in a two-dimensional histogram of E_1/W *vs.* E_2/W. A basis function calculated by a Monte Carlo simulation with fragment kinetic energies $\epsilon_1/W = 0.194$ and $\epsilon_2/W = 0.346$ is shown in (c). The dashed line indicates the kinematically accessible region in this plot.

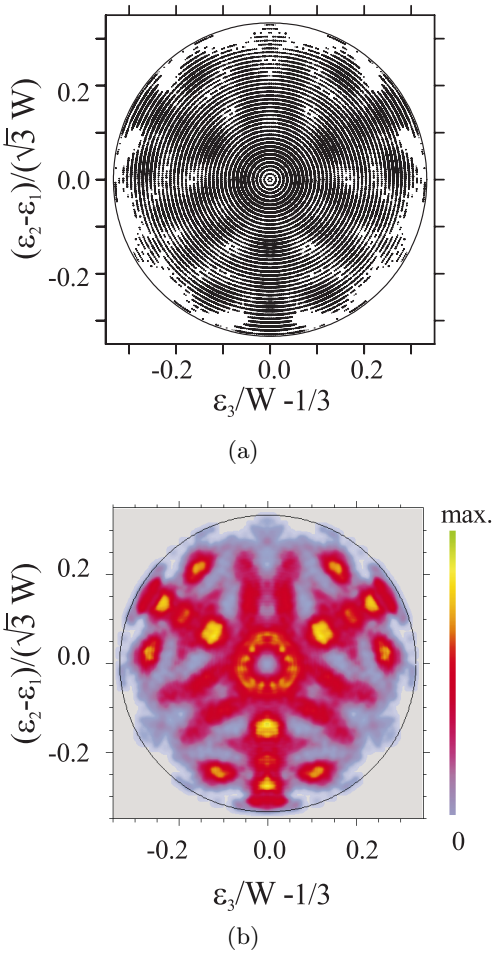

Fig. 8. Final state correlations of H_3 $3s\ ^2A_1'(N = 1, K = 0)$ three-body decay evaluated from double coincidences. The area of the squares in (a) is proportional to the weights of the basis functions. In (b), the final state distribution is shown in a false color plot.

The basis functions are calculated by a Monte Carlo simulation for sets of fixed fragment energies $(\epsilon_1, \epsilon_2, \epsilon_3 = W - \epsilon_1 - \epsilon_2)$ on a finely spaced grid in the kinematically accessible region of the phase space. In the simulation, the angle θ_f is distributed according to equation (4.1) with an alignment parameter $\beta_f = 2$, and the distributions of ψ_f and ϕ_f are uniform in $[0, 2\pi]$. The Monte Carlo simulation program calculates trajectories of the fragments, taking into account the finite size of the interaction region, the primary beam divergence, the size and shape of the detector, and the uncertainties of the time- and position measurements. The data reduction and projection of the simulated hit positions and time differences is identical to that applied to the measured data. The basis function $X_b(A, B; \epsilon_1/W = 0.194, \epsilon_2/W = 0.346)$ is shown in Figure 7c. Most of the intensity in the plot is localized in a single bin which corresponds to the fragment energies ϵ_1, ϵ_2. The density which is scattered along horizontal, vertical and diagonal lines is produced by those events which have been evaluated with the incorrect sign in equations (A.11).

The weights $a(\epsilon_1, \epsilon_2)$ are shown by the size of the squares in the Dalitz plot Figure 8a. Note that the basis functions already take the apparatus geometric collection efficiency into account. Therefore, Figure 8a is the final state distribution of the three-body decay. For better comparison with the distributions resulting from triple-coincidence measurements, the data set is shown as a false color map in Figure 8b. A boxcar smoothing over 7 neighboring pixels was applied to the plot to remove the modulations produced by the binning in Figure 8a. The structured regions of high and low point density in the plot correspond remarkably well to those observed in the triple hit data of Figure 5. Clearly, the results of the double- and triple-coincidence measurements are consistent. Moreover, the evaluation of double hit data allows us to explore the kinematically allowed range in the vicinity of the linear configuration (see Fig. 1b) when one of the fragment momenta is close to zero and fails to be detected in the triple hit experiment.

Our Monte Carlo simulation program allows us to calculate apparent spectra of the mass ratio Z in parallel with the basis functions for the three-body decay. The apparent spectrum of Z determined using the weight factors in Figure 8 is shown in Figure 6 spectrum (b). The simulation is in excellent agreement with the continuous contribution

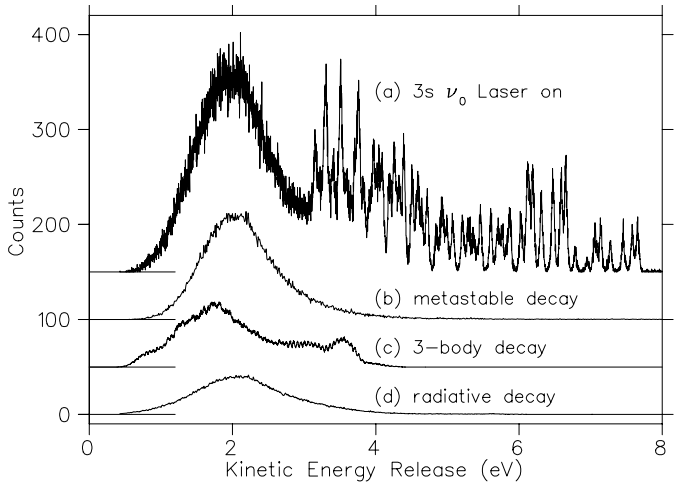

Fig. 9. Apparent two-body kinetic energy spectrum produced by H_3 $3s\ ^2A_1'(N=1,K=0)$. Legend: (a) measured spectrum of W with laser on, (b) spectrum produced by slow metastable decay, (c) simulated spectrum resulting from three-body decay, (d) continuum produced by radiative decay to ground state surface.

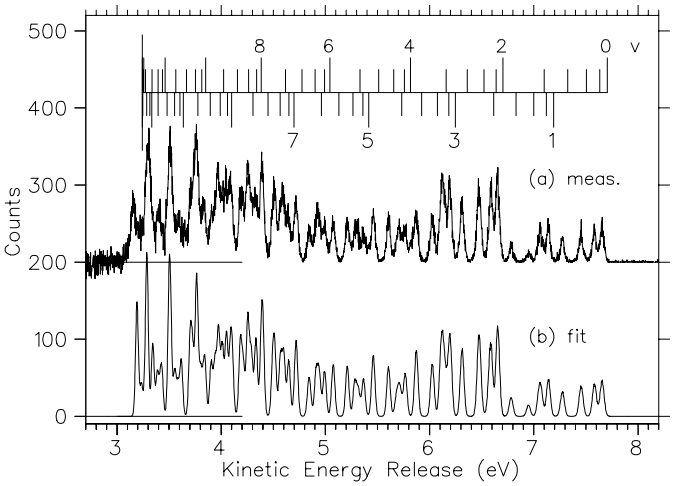

Fig. 10. Predissociation of H_3 $3s\ ^2A_1'(N=1,K=0)$. Legend: (a) measured spectrum, (b) fit with basis functions calculated by a Monte Carlo simulation. The sticks mark the rovibrational states of the H_2 fragment. Only ortho levels ($J=1,3,\dots$) are shown since only these appear in the spectrum.

observed in the measured spectrum. This shows that the three-body decay is consistently described. In addition, we find that a considerable fraction of the simulated three-body trajectories fulfills equation (4.3) and, therefore, appears as two-body decay. Our program allows us, to evaluate these trajectories and to predict the contribution in the two-body spectra which in fact originate from three-body decay.

4.2.2 Two-body decay of H_3

The events which fulfill equation (4.3) are evaluated as discussed in references [12,13]. The resulting spectrum of the (apparent) kinetic energy release W shown in Figure 9a contains contributions from:

- residual metastable decay,
- three-body decay with fragmentation configurations close to the H+H_2 limit,
- radiative decay to the ground state potential energy surface with subsequent dissociation into H+H_2 and,
- predissociation into H+$H_2(v,J)$.

The decay of the metastable $2p\ ^2A_2''$ state of H_3 produces a continuum in the kinetic energy release spectrum in the energy range between 0.5 and 5.5 eV with a maximum close to 2 eV. With the laser tuned to excite the $3s\ ^2A_1'$ state, an appreciable fraction of the population in the metastable state is depleted. The degree of depletion depends on the laser intensity and the overlap between the laser and the neutral beam. The procedure to determine the degree of depletion is described in Appendix B. Spectrum (b) in Figure 9 shows the properly scaled contribution of the metastable decay. The events resulting from three-body decay are estimated by the Monte Carlo simulation described in Section 4.2.1 and shown in spectrum (c) in Figure 9. To subtract the radiative decay, we follow the procedure described by Müller and Cosby [9]. We measure the W-spectrum of the $3d\ ^2E''$ state of D_3 and use this spectrum as a template for the radiative decay. In the case of D_3, the region in the potential energy surface occupied by the vibrational wave function is slightly smaller than that in H_3. This leads to a narrower distribution in the kinetic energy release spectrum. The radiative component for H_3 is shown in spectrum (d) in Figure 9.

The isolated discrete part in spectrum (a) is shown in Figure 10. We achieve an energy resolution of 50 meV which allows us to observe isolated peaks. They can be individually assigned to the rovibrational states of the $H_2(v,J)$ fragment. We observe clearly that only the H_2 states with odd angular momentum J and total nuclear spin $I_{\rm tot}=1$ (ortho states) are populated in predissociation. This is a consequence of the nuclear spin coupling in the vibrationless H_3 $3s\ ^2A_1'(N=1,K=0)$ initial state with $I_{\rm tot}=3/2$ [19]. The nuclear spin alignment is not altered in the predissociation process. The separation of one H-atom from H_3 in the quartet nuclear spin wave function ($I_{\rm tot}=3/2$) can only form H_2 in the triplet wave function ($I_{\rm tot}=1$). We fit the observed spectrum by a weighted sum of basis functions calculated for individual $H_2(v,J)$ final states by a Monte Carlo simulation. The fit shown in Figure 10b is in excellent agreement with the measured spectrum. The weights which correspond to the rovibrational population in the H_2 final state are shown in Figure 11. The distribution is in excellent agreement with that reported in a previous, independent investigation [9].

To compare our results with theoretical predictions, we project the rovibrational distribution on the vibrational axis. In Figure 12, we compare the measured vibrational distributions with the results of two-dimensional wave packet calculations by Schneider and Orel [17]. The new calculations [17] are in reasonable agreement with the experiment considering that the rotational degree of freedom cannot yet be tackled by theory. To achieve this high

Table 1. Branching between the fragmentation processes of H_3.

state	Two-body (H+H_2)		Three-body (H+H+H)
	radiative	predissociation	predissociation
$3s\ ^2A_1'(N=1,K=0)$, this work	6%	37%	57%
$3s\ ^2A_1'(N=1,K=0)$, exp. reference [10]	4%	37%	59%
$3s\ ^2A_1'$, theory[a] reference [17]		66%	34%
DR[b] at 10 meV reference [18]		25%	75%
DR at 5 eV reference [18]		65%	35%

[a] Two-dimensional wave packet calculation by Schneider and Orel [17] including accurate non-adiabatic coupling matrix elements. Ratio between two- and three-body predissociation rates. The radiative component is not included in the theory.
[b] Dissociative Recombination of H_3^+ with electrons.

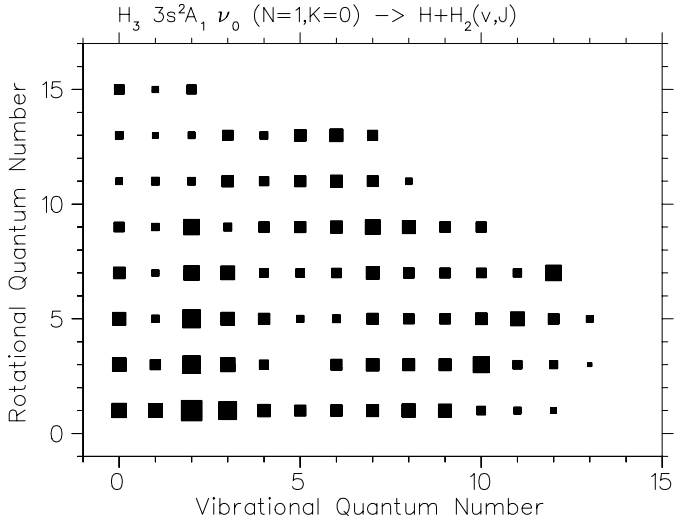

Fig. 11. Predissociation of H_3 $3s\ ^2A_1'(N=1,K=0)$: rovibrational population in the $H_2(v,J)$ fragment.

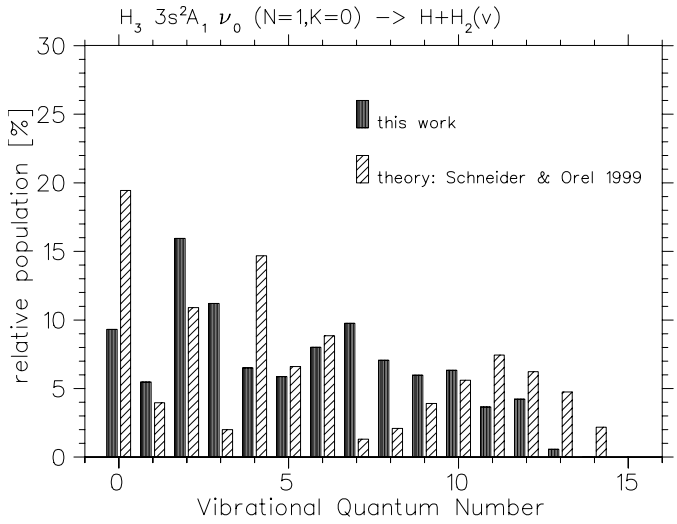

Fig. 12. Predissociation of H_3 $3s\ ^2A_1'(N=1,K=0)$: vibrational population in the $H_2(v)$ fragment. The measured distribution is compared to theoretical predictions by Schneider and Orel [17].

quality, the calculations had to explicitly include the non-adiabatic couplings between the potential energy surface of the laser-prepared initial state and the repulsive ground state. Only recently have such comprehensive calculations become possible due to the progress in computer power.

The simulations allow us to estimate the branching ratios between the fragmentation processes of the H_3 $3s\ ^2A_1'(N=1,K=0)$ state. The results are listed in Table 1. The results of this investigation are in good agreement with those in reference [10]. Three-body decay is the major fragmentation mechanism of H_3 $3s\ ^2A_1'(N=1,K=0)$. For completeness we quote branching values reported by theory for the $3s$ state and, those obtained in dissociative recombination (DR) at threshold and at 5 eV above threshold.

5 Conclusions

We have demonstrated the performance of the new Freiburg photofragment spectrometer which allows us to investigate laser-photodissociation of neutral molecules into two, three, or more neutral products. The fragments are detected in coincidence and their vectorial momenta in the final state are determined. We have analyzed the fragmentation of the vibrationless $3s\ ^2A_1'(N=1,K=0)$ state of the triatomic hydrogen molecule which decays by three competing processes: three-body decay into H+H+H, two-body predissociation into H+$H_2(v,J)$, and photoemission to the H_3 ground state surface with subsequent two-body decay. This state is an ideal object to develop and explore the data acquisition and analysis methods.

In the case of two-body predissociation, we have measured the rovibrational populations in the $H_2(v,J)$ fragment. The distributions are in excellent agreement with those from a previous investigation. The vibrational distributions of H_2 agree comparatively well with the results of a recent theoretical study. For three-body decay, we have acquired triple coincidences and determined the six-fold differential cross-section for the photodissociation process. We observe a strong angular alignment in the final state due to the anisotropy induced by the laser-excitation process. In the final state momentum correlations, we observe pronounced patterns which are characteristic for the dissociation mechanism. We have developed a Monte Carlo

simulation to determine the geometric collection efficiency of the detector and to correct the experimental raw data. We also show that for a three-body decay process with mono-energetic kinetic energy release, the detection of two fragments is sufficient to determine the final state momentum correlations. Although the data reduction algorithm is under-determined, missing information can be substituted by physically justified assumptions. To determine correct final state distributions, we apply a fitting technique with basis functions calculated by a Monte Carlo simulation which models the properties of the apparatus and the effect of the data reduction procedure. The final state distributions determined by this independent method agree extremely well with the direct results from triple-coincidence data. Moreover, this method allows us to fully explore the phase space of the final state and to determine the branching between the two- and three-body decay processes of H_3 $3s\ ^2A_1'(N=1,K=0)$.

This research was supported by Deutsche Forschungsgemeinschaft (SFB 276 TP C13). We thank Prof. Ch. Schlier (Univ. Freiburg) for carefully reading the manuscript.

Appendix A: Evaluation of three-body decay from double coincidence data

The parent molecules with mass M and translational energy E_0 of several keV propagate with velocity $\mathbf{v}_0 = (v_{0x}, v_{0y}, v_{0z})$ along the x-direction in the laboratory frame. The transverse components of $\mathbf{v}_0$ are much smaller than the longitudinal component ($v_{0y} \ll v_{0x}, v_{0z} \ll v_{0x}$). The dissociation into n fragments with masses m_i and center-of-mass velocities $\mathbf{u}_i = (u_{ix}, u_{iy}, u_{iz})$ is initiated in the laser-interaction region at the position (x_0, y_0, z_0). The positions (y_i, z_i) and the arrival time differences $(t_i - t_1)$ of the fragments in the plane $x = L$ are determined in the experiment. These quantities are related to the fragment velocities by the $3n$ equations of motion ($i = 1, 2, \ldots n$)

$$(v_{0x} + u_{ix})(t_i - t_0) + x_0 = L, \tag{A.1}$$
$$(v_{0y} + u_{iy})(t_i - t_0) + y_0 = y_i, \tag{A.2}$$
$$(v_{0z} + u_{iz})(t_i - t_0) + z_0 = z_i. \tag{A.3}$$

In a continuous beam experiment, the time of fragmentation t_0 is unknown. Data reduction strategies to determine the momenta of n fragments detected in coincidence have been developed by Beckert and Müller [13] and their implications for the evaluation of two- and three-body decay have been discussed by these authors.

In the following, we consider the special case of three-body decay with equal fragment masses $m = M/3$ and detection of only two of the three fragments in coincidence. The five quantities y_1, z_1, y_2, z_2 and $t_2 - t_1$ are measured by the detector. We neglect the primary beam divergence ($v_{0y} = v_{0z} = 0$) and the size of the interaction region ($x_0 = y_0 = z_0 = 0$). The longitudinal component v_{0x} is known from the kinetic energy $E_0 = Mv_{0x}^2/2$ of the primary molecular beam. The solution of equations (A.1–A.3) for ($i = 1, 2$) is

$$u_{ix} = L/(t_i - t_0) - v_{0x}, \tag{A.4}$$
$$u_{iy} = y_i/(t_i - t_0), \tag{A.5}$$
$$u_{iz} = z_i/(t_i - t_0). \tag{A.6}$$

The c.m. velocity components of the third fragment are determined using momentum conservation. To eliminate t_0, we assume that the kinetic energy release W_0 in the fragmentation process is monoenergetic and is known from an independent experiment. We express the total kinetic energy release $W_0 = m\sum_i \mathbf{u}_i^2/2$ in the form

$$u_{1x}^2 + u_{2x}^2 + u_{3x}^2 = 2W_0/m - \sum_{i=1}^{3} u_{iy}^2 + u_{iz}^2 \equiv u_{0x}^2 \tag{A.7}$$

with the abbreviation u_{0x}^2 for the right hand side in equation (A.7). We introduce the velocity differences d_{2x}:

$$d_{2x} \equiv u_{1x} - u_{2x} = (t_s - t_1)(v_{0x} + u_{sx})(v_{0x} + u_{1x})/L. \tag{A.8}$$

Using momentum conservation ($u_{1x} + u_{2x} + u_{3x} = 0$), we express u_{1x} and u_{2x} by u_{3x} and the velocity difference d_{2x}:

$$u_{1x} = (d_{2x} - u_{3x})/2; \quad u_{2x} = -(d_{2x} + u_{3x})/2. \tag{A.9}$$

We eliminate u_{1x} and u_{2x} in equation (A.7) and find for u_{3x}:

$$u_{3x} = \pm\sqrt{\left(2u_{0x}^2 - d_{2x}^2\right)/3}. \tag{A.10}$$

Two solutions exist because equation (A.7) remains invariant under a sign change of the u_{ix}.

From equations (A.5–A.10) we find an iterative procedure which involves all components of the fragment velocity vectors $\mathbf{u}_i$:

$$\begin{aligned}
u_{0x}^2 &= 2W_0/m - \sum_{i=1}^{3} u_{iy}^2 + u_{iz}^2 \\
d_{2x} &= (t_2 - t_1)(v_{0x} + u_{2x})(v_{0x} + u_{1x})/L \\
u_{3x} &= \pm\sqrt{\left(2u_{0x}^2 - d_{2x}^2\right)/3} \\
u_{1x} &= (d_{2x} - u_{3x})/2; \qquad u_{2x} = -(d_{2x} + u_{3x})/2 \\
u_{iy} &= y_i(v_{0x} + u_{ix})/L \quad i = 1, 2; \\
u_{3y} &= -u_{1y} - u_{2y} \\
u_{iz} &= z_i(v_{0x} + u_{ix})/L \quad i = 1, 2; \\
u_{3z} &= -u_{1z} - u_{2z}.
\end{aligned} \tag{A.11}$$

A suitable start vector is $\mathbf{u}_i = \mathbf{0}$ for $i = 1 \ldots 3$. Since we have to choose either the positive or the negative sign of the square root, the iteration (Eqs. (A.11)) converges

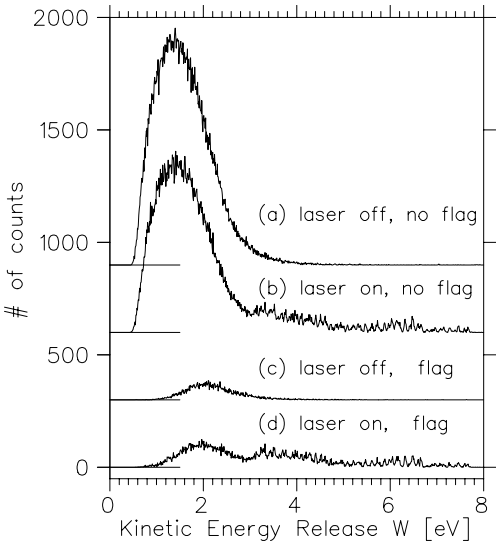

Fig. 13. Depletion of the H_3 metastable beam by laser-excitation to the H_3 $3s\ ^2A_1'(N=1,K=0)$ state. The apparent kinetic energy release spectra with (a) laser off, flag retracted, (b) laser on, flag retracted, (c) laser off, flag inserted, and (d) laser on, flag inserted are used to determine the degree of depletion (see text).

to the correct values of the fragment velocity vectors for 50% of the events. The algorithm is suitable to evaluate measured data. The effects of the finite beam divergence (v_{0y}, v_{0z}), the distribution of the point of dissociation (x_0, y_0, z_0), and the unknown sign in equations (A.11) can be modeled by a Monte Carlo simulation.

Appendix B: Depletion of the metastable beam

The decay of the metastable $2p\ ^2A_2''$ state of H_3 produces a continuum in the kinetic energy release spectrum in the energy range between 0.5 and 5.5 eV with a maximum close to 2 eV. In the resonant laser-excitation process, an appreciable fraction of the $2p\ ^2A_2''$ state population is excited and no longer contributes to this metastable signal. Hence, the laser-off spectrum has to be scaled before subtraction from the laser-on spectrum. If the metastable and the photofragment spectrum appear in totally different regions of the kinetic energy release spectrum, the scaling factor can easily be determined. In the case of laser-excited H_3, we observe a photoemission process with a kinetic energy release spectrum very similar to that of the metastable decay. The origin of the photofragments, however, is localized in the laser-intersection region. The metastable decay monitored by the detector is distributed over a comparatively large region downstream of the 300 μm aperture. The density of H_3 $2p\ ^2A_2''$ molecules decreases exponentially with a decay length $\lambda = v_0\tau$ of about 30 cm determined by the lifetime of the metastable state $\tau \approx 600$ ns [26] and the velocity of the fast beam v_0. In our apparatus, a beam flag mounted on a precision manipulator can be retracted and inserted reproducibly. With the beam flag inserted, the metastable beam is stopped in a distance of about 10 cm from the 300 μm aperture and, for the remaining part, the field of view for the detector is geometrically reduced. The collection efficiency for photofragments does not change with the beam flag inserted.

To determine the degree of excitation, we measure kinetic energy release spectra under the following conditions:

- laser on, flag inserted: $S_F^D(W)$,
- laser on, flag removed: $S^D(W)$,
- laser off, flag inserted: $S_F^N(W)$,
- laser off, flag removed: $S^N(W)$.

The four spectra are shown in Figure 13. Care must be taken to acquire the data under identical laser-excitation conditions. The spectra were normalized to the live time of the data acquisition system which was measured with a gated 5 MHz clock and a digital counter. The observed spectra contain contributions from metastable decay and photofragmentation. Generally, a spectrum $S(W)$ observed as a function of the apparent kinetic energy W is a convolution of the true spectrum $s(w)$ of the actual kinetic energy w with a kernel function $C(w, W)$. The kernel function depends on the geometry of the apparatus and the location of fragmentation. We define the normalized spectra of metastable decay and photofragmentation with and without beam flag:

$$S_m(W) = \int \mathrm{d}w\ s_m(w) C_m(w, W), \tag{B.1}$$

$$S_{mF}(W) = \int \mathrm{d}w\ s_m(w) C_{mF}(w, W), \tag{B.2}$$

$$S_p(W) = \int \mathrm{d}w\ s_p(w) C_p(w, W), \tag{B.3}$$

$$S_{pF}(W) = \int \mathrm{d}w\ s_p(w) C_{pF}(w, W). \tag{B.4}$$

The subscripts m and p label metastable decay and photofragmentation, respectively. Spectra with the flag inserted are labelled with an additional subscript F. The observed apparent spectra with/without laser and with/without beam flag $S_F^N(W)$, $S_F^D(W)$, $S^N(W)$, $S^D(W)$ are linear combinations of equations (B.1–B.4)

$$S^N(W) = I_m^0 S_m(W) \tag{B.5}$$

$$S^D(W) = (1-\alpha) I_m^0 S_m(W) + \alpha I_m^0 S_p(W) \tag{B.6}$$

$$S_F^N(W) = I_m^0 S_{mF}(W) \tag{B.7}$$

$$S_F^D(W) = (1-\alpha) I_m^0 S_{mF}(W) + \alpha I_m^0 S_{pF}(W) \tag{B.8}$$

with the total flux I_m^0 of metastable molecules passing the 300 μm aperture and the degree of dissociation α. In our apparatus, the collection efficiency for photofragments is solely determined by the detector geometry. No additional photofragment loss occurs with the beam flag inserted. As a consequence, the kernel functions for photofragments with and without beam flag are identical:

$$C_p(w, W) = C_{pF}(w, W). \tag{B.9}$$

We insert equation (B.9) into equations (B.5–B.8) and determine the differences between the spectra observed without and with beam flag:

$$S^D(W) - S_F^D(W) = I_m^0(1-\alpha)\int \mathrm{d}w\ S_m(w) \times \left(C_m(w,W) - C_{mF}(w,W)\right), \quad \text{(B.10)}$$

$$S^N(W) - S_F^N(W) = I_m^0\int \mathrm{d}w\ S_m(w) \times \left(C_m(w,W) - C_{mF}(w,W)\right). \quad \text{(B.11)}$$

Because an appreciable fraction of the metastable beam is intercepted by the flag, the kernel function without flag is considerably larger than that with the flag inserted $C_{mF}(w,W) \ll C_m(w,W)$. Therefore, the difference between the kernels in equations (B.10, B.11) is positive and we find α by

$$1-\alpha = \frac{S^D(W) - S_F^D(W)}{S^N(W) - S_F^N(W)}\cdot \quad \text{(B.12)}$$

The spectra shown in Figure 13 correspond to a depletion of $\alpha = 0.3$. The photofragment spectrum is then

$$S_F^D(W) - (1-\alpha)S_F^N(W) = I_m^0\alpha\int \mathrm{d}w S_{p0}(w)C_{pF}(w,W). \quad \text{(B.13)}$$

The identical spectrum appears from the relation $S^D(W) - (1-\alpha)S^N(W)$. In practice, however, the accuracy of equation (B.13) is higher.

References

1. I. Dabrowski, G. Herzberg, Can. J. Phys. **58**, 1238 (1980); G. Herzberg, J.K.G. Watson, Can. J. Phys. **58**, 1250 (1980); G. Herzberg, H. Lew, J.J. Sloan, J.K.G. Watson, Can. J. Phys. **59**, 428 (1981); G. Herzberg, J.T. Hougen, J.K.G. Watson, Can. J. Phys. **60**, 1261 (1982).
2. U. Müller, U. Majer, R. Reichle, M. Braun, J. Chem. Phys. **106**, 7958 (1997).
3. U. Müller, M. Braun, R. Reichle, R.F. Salzgeber, J. Chem. Phys. **108**, 4478 (1998).
4. R. Reichle, I. Mistrík, U. Müller, H. Helm, Phys. Rev. A **60**, 3929 (1999).
5. I. Mistrík, R. Reichle, U. Müller, H. Helm, M. Jungen, J.A. Stephens, Phys. Rev. A **61**, 033410 (2000).
6. I. Mistrík, R. Reichle, U. Müller, H. Helm, Phys. Rev. A **63**, 042711 (2000).
7. P.C. Cosby, H. Helm, Phys. Rev. Lett. **61**, 298 (1988).
8. J.R. Peterson, P. Devynck, Ch. Hertzler, W.G. Graham, J. Chem. Phys. **96**, 8128 (1992).
9. U. Müller, P.C. Cosby, J. Chem. Phys. **105**, 3532 (1996).
10. U. Müller, P.C. Cosby, Phys. Rev. A **59**, 3632 (1999).
11. U. Müller, Th. Eckert, M. Braun, H. Helm, Phys. Rev. Lett. **83**, 2718 (1999).
12. M. Braun, M. Beckert, U. Müller, Rev. Sci. Instrum. **71**, 4535 (2000).
13. M. Beckert, U. Müller, Eur. Phys. J. D **12**, 303 (2000).
14. S.E. Sobottka, M.B. Williams, IEEE Trans. Nucl. Sci. **35**, 348 (1988).
15. O. Jagutzki, V. Mergel, K. Ullmann-Pfleger, L. Spielberger, U. Meyer, H. Schmidt-Böcking, *SPIE Proc. "Imaging Spectroscopy IV"*, San Diego, 19-24 July 1998, Vol. 3764.
16. J.L. Krause, K.C. Kulander, J.C. Light, A.E. Orel, J. Chem. Phys. **96**, 4283 (1992); J.L. Krause, A.E. Orel, B.H. Lengsfield, K.C. Kulander, in *Time-Dependent Quantum Molecular Dynamics*, edited by J. Broeckhove, L. Lathouwers (Plenum, New York, 1992), p. 131.
17. I.F. Schneider, A.E. Orel, J. Chem. Phys. **111**, 5873 (1999).
18. S. Datz, G. Sundström, Ch. Biedermann, L. Broström, H. Danared, S. Mannervik, J.R. Mowat, M. Larsson, Phys. Rev. Lett. **74**, 896 (1995).
19. H. Helm, L.J. Lembo, P.C. Cosby, D.L. Huestis, *Fundamentals of Laser Interactions II*, Lecture Notes in Physics, edited by F. Ehlotzky (Springer, Berlin, 1989), p. 264.
20. R. Bruckmeier, Ch. Wunderlich, H. Figger, Phys. Rev. Lett. **72**, 2550 (1994); D. Azinovic, R. Bruckmeier, Ch. Wunderlich, H. Figger, Phys. Rev. A **58**, 1115 (1998).
21. A.B. Raksit, R.F. Porter, W.P. Garver, J.J. Leventhal, Phys. Rev. Lett. **55**, 378 (1985).
22. S. Mahapatra, H. Köppel, J. Chem. Phys. **109**, 1721 (1998).
23. R.H. Dalitz, Philos. Mag. **44**, 1068 (1953); Ann. Rev. Nucl. Sci. **13**, 339 (1963).
24. R.N. Zare, Ber. Bunsenges. Phys. Chem. **86**, 422 (1982).
25. A.R. Edmonds, *Angular Momentum in Quantum Mechanics* (Princeton University Press, 1960).
26. C. Bordas, P.C. Cosby, H. Helm, J. Chem. Phys. **93**, 6303 (1990).